# A HIGH-RESOLUTION SPATIOTEMPORAL INVESTIGATION OF CHESAPEAKE BAY WATER CLARITY WITH IMPLICATIONS FOR SEDIMENT TRANSPORT AND PRIMARY PRODUCTION

Jessica S. Turner[1]
Advisors: Marjorie A. M. Friedrichs[1] and Carl T. Friedrichs[1]
[1]Virginia Institute of Marine Science, William & Mary, Gloucester Point, VA 23062

## Abstract

While ecosystem health is improving in many estuaries worldwide following nutrient reductions, ambiguous trends in water clarity often remain. The Chesapeake Bay, a highly populated eutrophic estuary, is a crucial testbed for this issue. Efforts are needed to understand why downstream estuarine water clarity appears uncorrelated with watershed management actions, and these efforts require multiple metrics of clarity. To complement in situ measurements, satellite remote sensing provides an additional measurement platform to assess change over time. In this study, MODIS-Aqua remote sensing reflectance (Rrs) was evaluated from 2003-2020 at multiple wavelengths and spatial resolutions for surface waters of the Chesapeake Bay. Trends show an overall long-term darkening (decreased Rrs) in the upper estuary for all wavelengths yet brightening (increased Rrs) in the lower estuary for green wavelengths. Trends in band ratios show long-term decreasing red-to-green and red-to-blue ratios yet long-term increasing green-to-blue ratios. These trends are generally consistent with a long-term reduction in total suspended solids concentration without as clear a reduction in Chl-a. However, the spatial patterns in long-term trends for single bands (i.e., 645 nm) differ widely from the spatial patterns in trends in band ratios (i.e., 667/488), highlighting the importance of careful algorithm selection for long-term analysis of water clarity trends.

## 1. Introduction

Studying change in water clarity over time in estuaries is an integral part of assessing improvements from historically polluted conditions. Light availability in estuaries is a critical driver of primary production and ecosystem health, shaping important nursery habitats such as seagrass meadows, coral reefs, and oyster reefs. Low water clarity is often concurrent with pathogens and harmful algal blooms, impacting fisheries and human health. Many of the world's estuaries have experienced widespread eutrophication and degraded water clarity (*1*). Some estuaries have recovered from past degradation in recent years (*2*). Despite nutrient reductions and related improvements in ecosystem conditions (higher oxygen, increased seagrass), in many estuaries, water clarity results still do not align with watershed cleanup efforts (*3*–*5*).

The Chesapeake Bay (CB) serves as a prime case study for past eutrophication, recent improvements, and ambiguous clarity response requiring further analysis. In this estuary, water clarity is used in regional watershed management alongside chlorophyll-a (Chl-a) and oxygen to assess the health of the estuary (*6*), and watershed sediment and nutrient inputs are both actively managed for reduction (*7*). Clarity change following cleanup has been ambiguous: despite extensive management efforts and recent documentation of reductions in riverine nutrient inputs (*8*, *9*), water clarity as monitored in situ by Secchi disk depth has declined in the CB over the last 30 years (*10*–*14*). Current knowledge of water clarity from in situ observations fails to explain these incongruities. It is crucial that we understand the causes of discrepancies between management actions and water clarity results in the CB.

A more thorough understanding of the spatial and temporal patterns in water clarity metrics –

including remote sensing reflectance – is needed to understand why long-term water clarity trends do not reflect watershed nutrient reductions. Since in situ data is limited by spatial coverage, cruise frequency, and methods changes (*14*, *15*), satellite remote sensing data are needed. Remote sensors have been measuring surface reflectance for multiple decades and thus can substantially complement in situ programs.

The CB has served as a testbed for remote sensing research, including effective use of the Moderate-resolution Imaging Spectroradiometer on NASA Earth Observation satellite Aqua (MODIS-Aqua) to estimate water quality variables light attenuation ($K_d$), total suspended solids (TSS), Chl-a, absorption by colored dissolved organic matter ($a_{CDOM}$), and dissolved organic carbon (*16*–*26*). While most past studies focus on derived variables, uncertainties are high and may mask important particulate, planktonic, and dissolved contributions to long-term trends (*27*). Rrs values themselves have been used in other estuaries to explain general patterns (*13*, *28*), thus the Rrs approach is used in the present study for CB to study change over time.

This work expands upon past research in the CB by using Rrs rather than derived variables toward answering questions about change over time, in order to complement the ambiguous trends seen in situ. To date, there have been few studies of change over time in CB satellite-based remote sensing reflectance. Satellite estimates have been established for many water quality variables using multiple algorithms; however, these data are not often used to answer science questions about change over time in the mainstem Bay. Change over time has been investigated in cruise-based observations, yet in remote sensing, detailed analysis of long-term change has been limited to red-to-green ratio Chl-a (*24*), Rrs(645)-based clarity estimates (*29*), and mid-Bay Rrs(555) (*13*). Long-term trends have been heretofore unacknowledged for satellite Rrs at multiple bands and band ratios. Past studies of change over time in satellite-derived water quality, though useful, only extended to the early 2010s and focused on the mid-Bay; therefore, an estuary scale investigation of trends over time extending into recent years is required.

The objective of the proposed work is to quantify water clarity change in the CB mainstem over the past two decades via remote sensing reflectance (Rrs) and band ratios from MODIS-Aqua. Since the goal of the proposed work is to examine long-term temporal trends, the accuracy and precision of water clarity variable estimates are less important than overall patterns. That is, trends and patterns in the remote sensing data are useful in answering research questions despite potential biases in the values themselves. We aim to answer the questions: How have Rrs(λ) and band ratios changed over time in CB 2003-2020? What do those trends suggest in the context of long-term change?

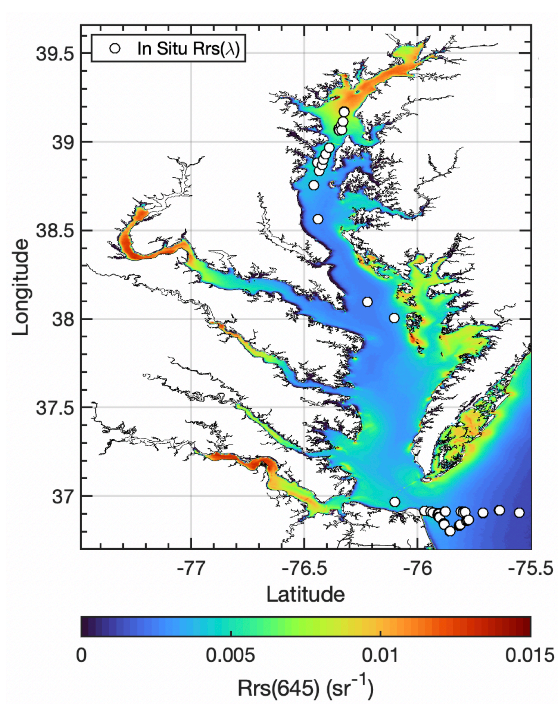


**Fig. 1** Map of MODIS-Aqua satellite data extent and in situ validation stations. Long-term mean Rrs(645) at 250m spatial res. is mapped in color. White points indicate in situ data locations (Table 1).

## 2. Methods

### 2.1. Study area

The CB is estuary drains an upstream watershed area of 116,000 km$^2$ with forested, agricultural, and urban land use in six states. The Bay is fed by multiple large tributary rivers and is generally shallow (mean depth of 7 m) with a deep central channel (> 30 m). In the present study, analysis focuses on the mainstem Bay and lower reaches of the large tributary rivers (Fig. 1). Spatially, satellite data points < 750 m from shore and in smaller tributaries were excluded, although often points farther from shore (~1 to 5 km) were also excluded due to additional data quality control, especially at 1km spatial resolution.

### 2.2. In situ Rrs data

To evaluate the Rrs satellite retrievals, we aggregated field observations in the mainstem CB obtained from the SeaWiFS Bio-optical Archive and Storage System (SeaBASS) (*30*, *31*). In situ, Rrs at the water surface is quantified from concurrent values of upwelling radiance and downwelling irradiance, using two connected radiometers pointing downward into the water column and upward at the sky. Thus, Rrs is the surface ratio of upwelling radiance emerging from water to downwelling radiative flux in air (*32*, *33*) in units of steradians (sr$^{-1}$). In situ Rrs measurements were reported from a wide range of times and locations throughout the mainstem Bay, including multiple seasons in years 2005 to 2014 (Fig. 1; Table 1).

**Table 1.** List of field measurements used for validation.

| Cruise | Time | n* | Reference |
|---|---|---|---|
| CB_Plume_D01 | May 2005 | 20 | (*25*, *34*) |
| CB_Plume_D02 | Nov 2005 | 2 | (*25*, *34*) |
| BIOME_B02 | Jul 2005 | 3 | (*25*, *34*) |
| GEO-CAPE | Jul 2011 | 29 | (*24*, *26*, *35*) |
| BOCP | Aug 2013 | 6 | (*36*) |
| CB Light Tower | 2005-2007 | 23 | (*37*, *38*) |
| CB Valid. Cruise | Aug 2013 | 1 | |
| SABOR | Jul 2014 | 1 | (*39*, *40*) |

*Paired data points for 250m spatial resolution.

### 2.3. Satellite Rrs data

MODIS-Aqua Rrs data from January 2003 to December 2020 were used to study long-term trends (Table 2), including ocean band and land band at visible wavelengths (*41*, *42*). Rrs at the water surface is calculated from the total radiance exiting the top of earth's atmosphere through a process of atmospheric correction (AC) to remove the contributions of aerosols (*43*, *44*), with subsequent removal of sun glint, whitecaps, and other artefacts. As a result, less than 10% of top-of-atmosphere reflectance is contributed by the ocean (*45*, *46*).

**Table 2.** MODIS-Aqua bands of interest for water quality studies in coastal and inland waters.

| Wavelength (nm) | Band | Bandwidth (nm) | Spatial res. (m) |
|---|---|---|---|
| 412 | 8 | 405-420 | 1000 |
| 443 | 9 | 438-448 | 1000 |
| 469 | 3 ^ | 459-479 | 500 |
| 488 | 10 | 483-448 | 1000 |
| 531 | 11 | 526-536 | 1000 |
| 547* | 12 | 546-556 | 1000 |
| 555 | 4 ^ | 545-565 | 500 |
| 645 | 1 ^ | 620-670 | 250 |
| 667 | 13 | 662-672 | 1000 |
| 678 | 14 | 673-683 | 1000 |

* Nominal band center for 547nm band is ~551nm.
^ Land band.

Data were processed from Level-1 through Level-3 using a custom merging method. Traditional AC in highly turbid waters may cause data loss as bright sediment-laden waters alias as atmospheric haze or clouds due to high emission in the infrared, biasing aquatic retrievals toward low-turbidity conditions and underrepresenting data due to missing pixels. Therefore, a custom AC using shortwave infrared and near-infrared (SWIR/NIR) merging method was used to ensure that the high-turbidity data were included in the analysis. Following the methods of Aurin et al. (*47*) we used two AC methods, SWIR for high turbidity (HT) and NIR for low turbidity (LT) pixels, processing each scene to level-2 using both separate AC methods and then merging those scenes. For HT, we added the mode offset for non-high-light pixels back to each entire scene. The present study diverged from Aurin et al. (*47*) in that the median negative offset was not added back to level-2 LT scenes, as it caused misalignment of Rrs values for the same band at different spatial resolutions (e.g., 555 nm). Spatially, HT and LT Rrs data were processed to level-2 at the nominal spatial resolution of each band. Rrs(645) was processed to all spatial resolutions in order to facilitate the merging method. At all spatial resolutions, we merged the scenes along spatial guidelines set by Rrs(645) threshold value of 0.01 $sr^{-1}$ by adding the LT pixels to the HT scene where Rrs(645) < 0.01 $sr^{-1}$ to create the level-2B scene. Using these merging methods, up to twice as many scenes per month were included in monthly averages. Custom-processed level-2B Rrs scenes were binned to level-3 monthly composites at the respective spatial resolutions for each band to facilitate trend analysis over a consistent spatial grid.

Although many scenes were excluded from the dataset due to clouds and other artefacts, no seasonal bias in cloud cover was found. Approximately 4 to 8 scenes were included in each monthly composite. The number of points in monthly composites showed only very small variation between spatial resolutions, quantified by comparing Rrs(645) level-3 mapped images for 250m, 500m, and 1km spatial resolutions. The slight decrease in points per month with coarsening spatial resolution was most relevant to coast-adjacent pixels, for which long-term trends were not analyzed in the current study.

## 2.4. Validation

Validation of MODIS-Aqua Rrs for the CB region was performed using SeaBASS datasets 2005 to 2014 (Table 1). Matchups all fell within 6 hours of a MODIS-Aqua overpass. Satellite data at station locations were extracted via slightly different spatial matchup windows depending on the spatial resolution of the level-3 file, using an aerial coverage of approximately 1.6, 2.25, and 1 $km^2$ for the three respective spatial resolutions 250m, 500m, and 1km. Rrs values were compared by individual bands at each wavelength's nominal spatial resolution (Table 3) and at 1km (Fig. 2). Metrics for satellite skill assessment included the mean ratio, bias, mean absolute error (MAE), root mean squared error (RMSE), mean absolute percent difference (mean APD), and correlation coefficient (R).

## 2.5. Calculation of long-term trends

Monthly composite images were used for trend analysis to maximize spatial coverage and use a constant temporal sampling interval for each year. Due to the spatial resolution characteristics of time series dataset (Table 2), analysis of trends in single bands used the nominal spatial resolution of each band. Analysis of trends in band ratios used the coarsest common spatial resolution of the two wavelengths in question, depending on band ratio shown. For example, Rrs(555)/Rrs(645) trends were calculated at 500m spatial resolution (the coarsest spatial resolution of those two bands), while trends in most band ratios, such as Rrs(667)/Rrs(488), were calculated at 1km spatial resolution. At each wavelength and for each band ratio, spatially-explicit trends were calculated for level-3 pixel locations (mapped/binned coordinates) that contained data for > 80% of the months in the time series from 2003 to 2020, i.e., > 173 of 216 monthly images. Trends were calculated as linear regressions using the slope of the least squares fit (i.e., *48*). Meaningful trends were assigned using an alpha level 90% confidence, i.e., $p < 0.1$.

# 3. Results

## 3.1. Validation results

Comparison with in situ Rrs revealed generally close matches between satellite-derived Rrs and observed conditions. Overall satellite Rrs very slightly underestimated in situ Rrs, with overestimation in the blue

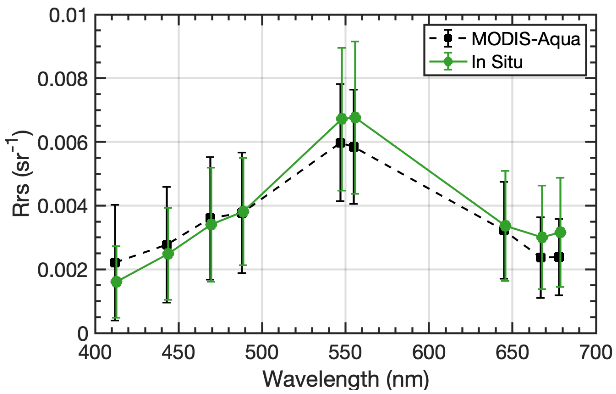

**Fig. 2** Mean and standard deviations of Rrs(λ) validation data points derived from MODIS-Aqua and measured in situ (n = 63), spanning multiple seasons and years 2005 to 2013. MODIS-Aqua values represent the means and standard deviations for single-pixel validation points at 1km spatial resolution.

wavelengths (< 488 nm) and underestimation in the green through red wavelengths (> 488 nm) (Table 3, Fig. 2). Skill was high for specific single bands, for example, the closest match to in situ Rrs was measured at 488 nm and 645 nm (Fig. 2). There was a small effect of spatial resolution on skill of satellite Rrs retrieval. Although satellite Rrs(645) was consistently lower than in situ Rrs(645), skill of satellite Rrs(645) decreased with coarsening spatial resolution (Table 3).

**Table 3.** Validation of Rrs(λ) for relevant MODIS-Aqua bands using in situ observed Rrs(λ) vs. corresponding daily (<6 hours) satellite scene pixels or pixel window averages, including multiple skill metrics.

| Band (nm) | Spatial res. | n | Mean ratio | Bias | MAE | RMSE | Mean APD | R |
|---|---|---|---|---|---|---|---|---|
| 412 | 1 km | 63 | 1.4 | 0.0006 | 0.0013 | 0.0016 | 37% | 0.58 |
| 443 | | 63 | 1.1 | 0.0003 | 0.0010 | 0.0014 | 12% | 0.67 |
| 488 | | 63 | 1.0 | 0.00004 | 0.0010 | 0.0013 | 1% | 0.75 |
| 531 | | 63 | 1.0 | -0.0002 | 0.0012 | 0.0015 | 1% | 0.67 |
| 547 | | 63 | 0.9 | -0.0007 | 0.0015 | 0.0020 | 7% | 0.61 |
| 645 | | 63 | 0.8 | -0.0007 | 0.0012 | 0.0015 | 15% | 0.70 |
| 667 | | 63 | 0.8 | -0.0006 | 0.0010 | 0.0013 | 17% | 0.70 |
| 678 | | 63 | 0.8 | -0.0008 | 0.0011 | 0.0014 | 19% | 0.72 |
| 469 | 500 m | 81 | 1.1 | 0.0002 | 0.0010 | 0.0014 | 15% | 0.73 |
| 555 | | 81 | 0.9 | -0.0009 | 0.0016 | 0.0021 | 9% | 0.60 |
| 645 | | 81 | 0.8 | -0.0006 | 0.0011 | 0.0015 | 12% | 0.66 |
| 645 | 250 m | 85 | 1.0 | -0.0001 | 0.0011 | 0.0014 | 6% | 0.65 |

### 3.2. Change over time in Rrs at single bands

Generally, Rrs at all wavelengths decreased over time in the upper Bay and increased in the lower Bay, although the spatial extent, magnitude, and meaningfulness of those trends varied among wavelengths (Fig. 3). For the 412 nm band, the upper Bay region saw long-term meaningful decreases in Rrs, with the region of decreasing Rrs extending down-estuary to the Rappahannock shoal. However, Rrs(412) in the lower Bay increased over time at scattered locations near the eastern Bay and Bay mouth (Fig. 3a). Rrs(443) decreased over time in the upper Bay with the region of long-term decrease extending to the latitude of the Potomac river mouth. Rrs(443) showed long-term increases in the lower Bay from the Bay mouth up-estuary on the eastern side of the Bay to Tangier island (Fig. 3b). Long-term decreases in Rrs(469) were found throughout the mainstem Bay north of the Potomac river; meanwhile, increases over time were found near the Bay mouth (Fig. 3c), though not as spatially extensive as the increases found for Rrs(443) or Rrs(488). For blue wavelengths (412, 443, and 469 nm) long-term decreases were also seen in the lower Potomac River. Rrs(488) decreased in the upper Bay, followed by an area of no trend, with an additional small region of decreasing Rrs(488) at the latitude of the mouth of the Patuxent river. Larger magnitude (>0.0001 sr$^{-1}$ yr$^{-1}$) increases in

Rrs(488) were found for most of the lower Bay, extending spatially up-estuary to Tangier island and reaching east-to-west across most of the mainstem Bay (Fig. 3d). Upper Bay decreases and lower Bay increases in Rrs(531,547,555) (Fig. 3e-g) closely resembled spatial patterns in Rrs(488), except all three green wavelengths additionally showed a region of meaningful long-term increase in Rrs in the lower James River. Decreases in Rrs(645) were found in the upper Bay extending down-estuary to just above the Choptank River mouth, with an additional small region of decreased Rrs(645) level with the mouth of the Patuxent River. Most of the lower Bay lacked any long-term trend in Rrs(645), except for a region of large-magnitude decrease in the James River (Fig. 3h). Rrs(667) and Rrs(678) showed a few decreasing areas in the upper Bay, a few increasing areas near the Bay mouth, yet overall few meaningful trends (Fig. 3i, 6j). In short, a darkening (lower Rrs over time) was found for the upper Bay and some tributary rivers, especially at 469nm, while a brightening (higher Rrs over time) was found for the lower Bay Rrs, particularly at the green wavelengths (488, 531, 547, and 555 nm)

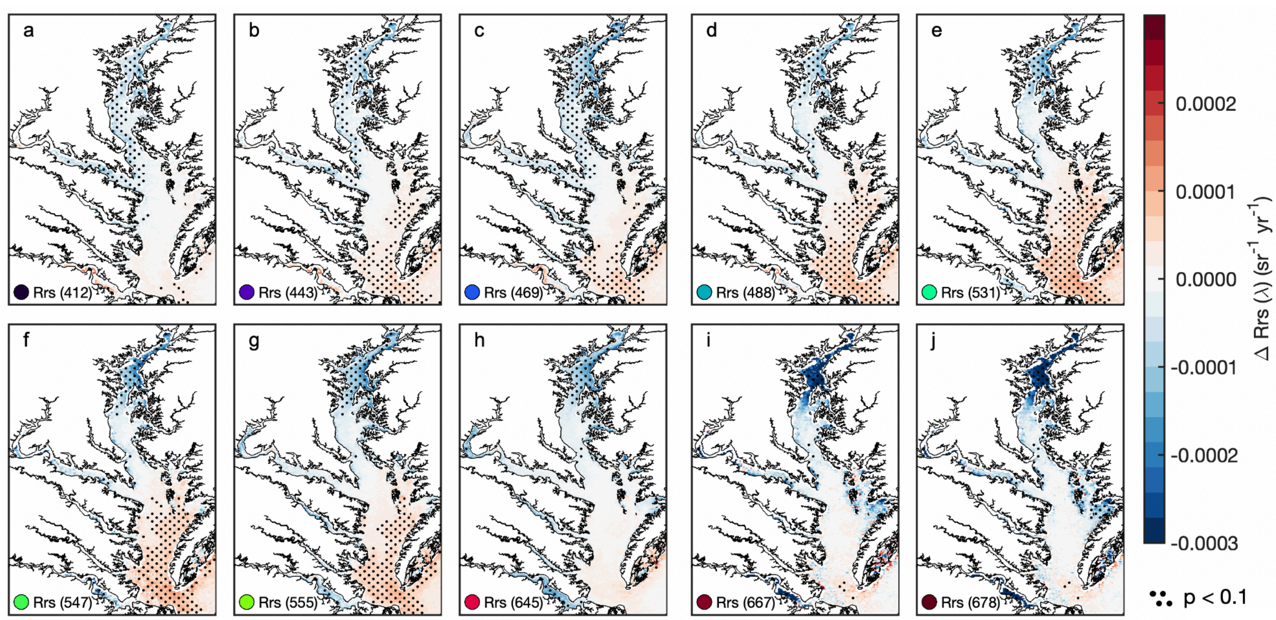


**Fig. 3** Trends over time in Rrs(λ) from 2003 to 2020 for bands 412 nm through 687 nm according to least-squares fits over all pixels with >80% of monthly images at the nominal spatial resolution of each band, i.e., h) Rrs(645) at 250m, c) Rrs(469) and g) Rrs(555) at 500m, and all other bands at 1km. Small black dots indicate statistically meaningful trends ($p < 0.1$).

3.3. Change over time in band ratios

Band ratios showed a wide range of results, with many showing heterogeneous spatial patterns in increases and decreases over time. Overall, multiple red-to-green ratios and red-to-blue ratios showed consistent, spatially widespread decreases (Fig. 4a,b), while some green-to-blue ratios showed consistent, spatially widespread increases (Fig. 4c). Long-term decreases were found throughout the mainstem Bay for eight red-to-green band ratios (Table 4). The largest magnitude and most spatially widespread decreases of these eight ratios were Rrs(645)/Rrs(531) (Fig. 4a), Rrs(645)/Rrs(547), and Rrs(678)/Rrs(547). Similarly, long-term decreases for three red-to-blue ratios were observed (Table 4). The largest magnitude decrease ($< -0.005$ $yr^{-1}$) was seen for Rrs(645)/Rrs(488), for which the region of decrease extended from the Bay mouth up-estuary to the eastern Bay above the Potomac River mouth (Fig. 4b). In contrast, long-term increases were observed for four green-to-blue ratios. Of these increasing green-to-blue band ratios, the trend in Rrs(488)/Rrs(469) was the largest in magnitude and most spatially widespread, reaching from the Bay mouth through almost the entire estuary (Table 4). Rrs(531)/Rrs(469) also showed widespread increasing trends from the Bay mouth up-estuary to the Patuxent River mouth (Fig. 4c).

**Table 4.** Trends over time in band ratios.

| Ratio type | $\lambda_1$ | $\lambda_2$ | Trend* | $Perc_{Bay}$** |
|---|---|---|---|---|
| Red-to-green | 678 | 555 | – | 30% |
| | 645 | 555 | – | 29% |
| | 678 | 547 | – | 30% |
| | 667 | 547 | – | 20% |
| | 645 | 547 | – | 32% |
| | 678 | 531 | – | 33% |
| | 667 | 531 | – | 25% |
| | 645 | 531 | – | 34% |
| Red-to-blue | 645 | 488 | – | 30% |
| | 667 | 488 | – | 21% |
| | 678 | 488 | – | 26% |
| Green-to-blue | 555 | 469 | + | 20% |
| | 531 | 469 | + | 33% |
| | 488 | 469 | + | 52% |
| | 547 | 469 | + | 26% |

* Where – or + indicate long-term decrease or increase.
**Percent of water pixels analyzed exhibiting a meaningful long-term trend ($p < 0.1$).

## 4. Discussion

### 4.1. Relevance to established algorithms

Using a red-band approach, i.e., Rrs(645) at 250m, we found a long-term decrease in the upper Bay and James River but no trend in most of the mainstem Bay (Fig. 3h). This red-band approach has historically been the most widely used index of water clarity in CB and estuaries with similar turbidity conditions (*19*, *49*). Our findings suggest that clarity is improving more substantially in the upper Bay than the lower Bay, according to the single-band red-Rrs approach.

Red-to-green ratios have been used in past studies of estuaries to estimate Chl-a, TSS, and turbidity; our findings would suggest a decrease in these variables over time for the mainstem Bay. Le et al.(*24*) used a “red-green chlorophyll index (RGCI)” based on the ratio Rrs(667)/Rrs(531) later employed by Ioannou et al. (*50*). In our study, we found that the relevant band ratio for this RGCI has decreased over time in the lower Bay, albeit with some spatial heterogeneity (Fig 7g). Reisinger et al.(*51*) used the red-to-green ratio Rrs(645)/Rrs(555) to estimate TSS in order to analyze a long time series in the coastal waters of the northern Gulf of Mexico. The corresponding ratio in our study (Fig. 4b) showed spatially widespread decreases over time for the mainstem CB, especially between the mainstem and eastern Bay south of the Patuxent River and north of the mouth of the James. Wang et al. (*52*) analyzed turbidity in the Pearl River estuary using a red-to-green ratio algorithms which, in our results, shows a long-term decrease (Table 4). Together, these findings suggest a potential improvement in water clarity over time according to red-to-green Rrs band ratios.

Red-to-blue ratios have related closely to in situ Kd and TSS in past studies; from our results, decreasing red-to-blue ratios may indicate improved water clarity over time, particularly in the lower Bay. Wang et al. (*16*) estimated a Kd(490) product for coastal waters based on the underlying band ratio Rrs(667)/Rrs(488), which, calibrated to in situ TSS-Kd relationships, also estimated CB TSS with relatively high skill (*22*). Siswanto et al. (*53*) independently used the same band ratio, Rrs(667)/Rrs(488), to estimate TSS in the East China Sea. In the present study, results show that this particular band ratio is decreasing in the lower CB, yet trends are spatially patchy (Table 4). Other previously used red-to-blue ratio water clarity algorithms did not yield meaningful trends over time in our analysis. For example, a high-resolution Kd(490) product developed for the CB (*54*) employing the ratio Rrs(645)/Rrs(469) did not yield any spatially consistent nor meaningful trends over time in our results. In short, red-to-blue ratios suggest that water clarity is improving, especially in the lower Bay, yet conclusions are less strongly supported than for red-to-green ratio findings.

Green-to-blue band ratios are related to algorithms used to retrieve both $a_{CDOM}$ and Chl-a. For example, O'Reilly et al. (*55*) describe the OC2 algorithm, which can additionally be used to estimate Chl-a from high-resolution (500m) MODIS imagery with the band ratio Rrs(555)/Rrs(469). The results of the present study point to a long-term increase in CB for the band ratio relevant to this Chl-a algorithm (Fig. 5b). These results suggest a long-term increase in Chl-a as measured by green colored pigment concentration.

4.2. Implications

Considering improvements to nutrient and sediment loading to the Bay, the estuary likely has two different responses to nutrients vs. sediments, as evidenced by long-term trends. The results of the present study show that Rrs(645), the most commonly used for water clarity variables, is decreasing over time in the upper Bay and the James River (Fig. 3h). These results may indicate that decreasing watershed sediment inputs may be realized in the more turbid sections of the Bay closest to river inputs. Also, red-to-green and red-to-blue ratios suggest improved water clarity in our results (Table 4). However, reduced sediment inputs do not always directly improve water clarity in the Bay according to all metrics. Modeling studies show that decreased sediment inputs can increase light availability to enhance organic matter production, increasing the concentration of organic suspended solids in surface waters in the mid-Bay (*56*). Therefore, while watershed nutrient reductions have parallel consequences in the downstream estuary, watershed sediment reductions could co-occur with seemingly misaligned effects in

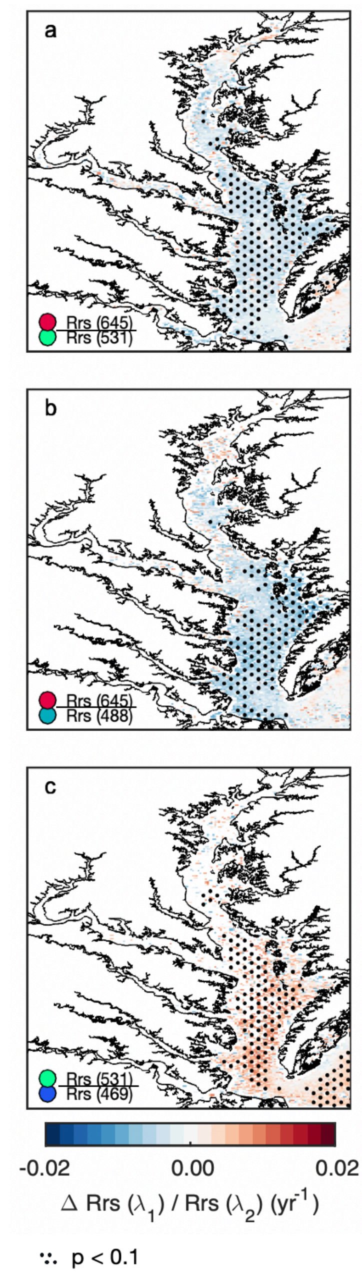


**Fig. 4** Example trends over time in band ratios, including a) red-to-green, b) red-to-blue, and c) green-to-blue ratios.

the estuary. The results of our work partially support this theory, since Rrs in the green bands (Fig. 3) and green-to-blue ratios (Fig. 4c) were found to be increasing over time in the lower Bay.

No two estuaries are alike, and underlying geology may play a strong role in a given region's optical complexity and subsequent success of water quality satellite retrievals. The use of region-specific analyses is critical, especially when management entities may incorporate more remote sensing for future decision making. The CB is not only optically complex, but the optically active constituents themselves are geochemically complex due to the geology and hydrology of the region. Other coastal regions such as Long Island Sound (*57*, *58*) show successful retrievals of Rrs-derived variables, even with highly variable river inputs, but only if the constituent type is homogenous for that region. This homogeneity of constituents, common in northern latitudes that have experienced glacial scour, lends itself to more accurate empirical relationships between Rrs and water quality variables. The same cannot be said of the CB, whose tributary rivers drain multiple diverse watersheds. The watershed of the CB includes rocky uplands and coastal plains with very different underlying geologies that lead to varied river chemistry (*59*) and likely to diverse types of dissolved and particulate matter entering the Bay from the different tributary rivers.

Results of this study show that the time scale of a given research question is critical for algorithm selection in optically complex estuarine waters. In contrast to studying long-term trends in the CB, short-term applications of remote sensing data can provide powerful insights. Impactful short-term uses for satellite remote sensing in the Bay include aquaculture siting and monitoring, comparing coastal bays, river plume extents, and other focused applications. The results of this study further support the idea that at long time scales, remote sensing of water clarity can complement, but not replace, in situ monitoring.


## Acknowledgments

The authors thank Bruce Monger, Dirk Aurin, Blake Clark, and Antonio Mannino for feedback on satellite data processing methods and general advice. Discussions with students of the Ocean Optics class of summer 2019, members of the NASA interagency CB working group, and members of the PACE Early Adopters group greatly helped this work. Ocean color data can be found on the NASA ocean color web Level 1&2 Data browser (https://oceancolor.gsfc.nasa.gov/cgi/browse.pl?sen=am). In situ Rrs data can be found on the NASA SeaBASS data archive (https://seabass.gsfc.nasa.gov/).


## Literature Cited


1. J. E. Cloern, *Mar. Ecol. Prog. Ser.* **210**, 223–253 (2001).
2. J. E. Cloern, A. D. Jassby, *Rev. Geophys.* **50** (2012), doi:10.1029/2012RG000397.
3. C. M. Duarte, D. J. Conley, J. Carstensen, M. Sánchez-Camacho, *Estuaries and Coasts*. **32**, 29–36 (2009).
4. D. F. Boesch, *Front. Mar. Sci.* **6** (2019), doi:10.3389/fmars.2019.00123.
5. C. Buchanan, *Estuaries and Coasts*. **43**, 661–679 (2020).
6. P. J. Tango, R. A. Batiuk, *J. Am. Water Resour. Assoc.* **49**, 1007–1024 (2013).
7. G. W. Shenk, L. C. Linker, *J. Am. Water Resour. Assoc.* **49**, 1042–1056 (2013).
8. J. S. Lefcheck *et al.*, *Proc. Natl. Acad. Sci.* **115**, 3658–3662 (2018).
9. Q. Zhang *et al.*, *Front. Mar. Sci.* **5**, 422 (2018).
10. L. W. Harding *et al.*, *Estuaries and Coasts*. **39**, 664–681 (2016).
11. J. M. Testa, V. Lyubchinch, Q. Zhang, *Estuaries and Coasts* (2019), doi:https://doi.org/10.1007/s12237-019-00547-9.
12. Q. Zhang, D. C. Brady, W. R. Boynton, W. P. Ball, *J. Am. Water Resour. Assoc.* **51**, 1534–1555 (2015).
13. C. L. Gallegos, P. J. Werdell, C. R. McClain, *J. Geophys. Res. Ocean.*, in press, doi:10.1029/2011JC007160.
14. M. R. Williams, S. Filoso, B. J. Longstaff, W. C. Dennison, *Estuaries and Coasts*. **33**, 1279–1299 (2010).
15. A. J. Bever, M. A. M. Friedrichs, C. T. Friedrichs, M. E. Scully, L. W. J. Lanerolle, *J. Geophys. Res. Ocean.* **118**, 4924–4944 (2013).
16. M. Wang, S. H. Son, L. W. Harding, *J. Geophys. Res. Ocean.* **114** (2009), doi:10.1029/2009JC005286.
17. M. Hasan, L. Benninger, *Estuar. Coast. Shelf Sci.* **191**, 136–149 (2017).
18. S. R. Signorini *et al.*, *J. Geophys. Res. Ocean.*

**124**, 3755–3778 (2019).
19. M. Ondrusek *et al.*, *Remote Sens. Environ.* **119**, 243–254 (2012).
20. N. DeLuca, B. Zaitchik, F. Curriero, *Remote Sens.* **10**, 1393 (2018).
21. G. Zheng, P. M. Digiacomo, S. S. Kaushal, M. A. Yuen-Murphy, S. Duan, *Environ. Sci. Technol.* **49**, 6494–6503 (2015).
22. S. Son, M. Wang, *Remote Sens. Environ.* **123**, 163–174 (2012).
23. P. J. Werdell *et al.*, *Remote Sens. Environ.* **113**, 1319–1330 (2009).
24. C. Le, C. Hu, J. Cannizzaro, H. Duan, *Estuar. Coast. Shelf Sci.* **128**, 93–103 (2013).
25. A. Mannino, M. E. Russ, S. B. Hooker, *J. Geophys. Res. Ocean.* **113**, C07051 (2008).
26. F. Cao *et al.*, *Remote Sens. Environ.* **205**, 151–165 (2018).
27. G. Zheng, P. M. DiGiacomo, *Prog. Oceanogr.* **159**, 45–72 (2017).
28. J. Tao, P. S. Hill, *J. Geophys. Res. Ocean.* **124** (2019), doi:10.1029/2019JC015336.
29. B. C. Crooke, L. McKinna, I. Cetinic, *Opt. Express*. **25**, A361–A374 (2017).
30. P. J. Werdell, S. W. Bailey, *NASA Tech. Memo.* **2002–21161**, 1–50 (2002).
31. P. J. Werdell *et al.*, *EOS, Trans. Am. Geophys. Union*. **84** (2003), doi:10.1029/2003EO380001.
32. J. E. O'Reilly *et al.*, *J. Geophys. Res.* **103**, 24937–24953 (1998).
33. C. D. Mobley *et al.*, *Appl. Opt.* **44**, 3576–3592 (2005).
34. A. Mannino, M. G. Novak, S. B. Hooker, K. Hyde, D. A. Aurin, *Remote Sens. Environ.* **152**, 576–602 (2014).
35. M. Zhang, C. Hu, J. Cannizzaro, M. G. Kowalewski, S. J. Janz, *Estuar. Coast. Shelf Sci.* **200**, 181–193 (2018).
36. A. Gilerson *et al.*, *Proc. SPIE*. **9638**, 96380A (2015).
37. G. Zheng, D. Stramski, *J. Geophys. Res. Ocean.* **118**, 2155–2174 (2013).
38. X. Pan, thesis, Old Dominion University (2007).
39. M. Ottaviani *et al.*, *Remote Sens. Environ.* **206**, 375–390 (2018).
40. A. P. Chase, E. Boss, I. Cetinić, W. Slade, *J. Geophys. Res. Ocean.* **122**, 9725–9743 (2017).
41. L. Feng, C. Hu, J. Li, *Water Resour. Res.* **54**, 3583–3601 (2018).
42. B. A. Franz *et al.*, *Proc. Ocean Opt.* (2006).
43. H. R. Gordon, M. Wang, *Appl. Opt.* **33**, 443–452 (1994).
44. Z. Ahmad *et al.*, *Appl. Opt.* **49**, 5545–5560 (2010).
45. S. Martin, *An Introduction to Ocean Remote Sensing* (Cambridge University Press, ed. 2nd, 2014).
46. J. T. O. Kirk, *Light and Photosynthesis in Aquatic Ecosystems* (Cambridge University Press, Cambridge, ed. 3rd, 1994).
47. D. A. Aurin, A. Mannino, B. Franz, *Remote Sens. Environ.* **137**, 212–225 (2013).
48. C. A. Greene *et al.*, *Geochemistry, Geophys. Geosystems*. **20**, 3774–3781 (2019).
49. Z. Chen, C. Hu, F. Muller-Karger, *Remote Sens. Environ.* **109**, 207–220 (2007).
50. I. Ioannou *et al.*, *Proc. SPIE*. **9111**, 911118 (2014).
51. A. Reisinger, J. C. Gibeaut, P. E. Tissot, *Front. Mar. Sci.* **4**, 233 (2017).
52. J. Wang *et al.*, *J. Geophys. Res. Ocean.* (2021).
53. E. Siswanto *et al.*, *J. Oceanogr.* **67**, 627–650 (2011).
54. M. C. Tomlinson, R. P. Stumpf, R. L. Vogel, *Remote Sens. Lett.* **10**, 178–185 (2019).
55. J. E. O'Reilly *et al.*, in *SeaWiFS Postlaunch Calibration and Validation Analyses, Part 3* (2000), pp. 8–22.
56. J. S. Turner, P. St-Laurent, M. A. M. Friedrichs, C. T. Friedrichs, *Sci. Total Environ.* **769** (2021), doi:10.1016/j.scitotenv.2021.145157.
57. D. A. Aurin, H. M. Dierssen, M. S. Twardowski, C. S. Roesler, *J. Geophys. Res. Ocean.* **115** (2010), doi:10.1029/2009jc005837.
58. D. A. Aurin, H. M. Dierssen, *Remote Sens. Environ.* **125**, 181–197 (2012).
59. R. G. Najjar *et al.*, *J. Geophys. Res. Ocean.* **125** (2020), doi:10.1029/2019JC015597.